Solid State Nuclear Magnetic Resonance 142 (2026) 102075

Contents lists available at ScienceDirect

Solid State Nuclear Magnetic Resonance

journal homepage: www.elsevier.com/locate/ssnmr

From overlap to resolution: Cellular solid-state NMR at ultrahigh-field 1.5 GHz demonstrated on fungal cell walls

Malitha C. Dickwella Widanage [a,b,*,1], Ankur Ankur [a,1], Bennett Addison [b], Ivan Huang [c], Xiaoling Wang [c,2], Peter L. Gor'kov [c], Zhehong Gan [c], Anne E. Harman-Ware [b], Tuo Wang [a,**]

[a] Department of Chemistry, Michigan State University, East Lansing, MI, USA
[b] Renewable Resources and Enabling Sciences Center, National Lab of the Rockies, Golden, CO, USA
[c] National High Magnetic Field Laboratory, Florida State University, Tallahassee, FL, USA

ARTICLE INFO

Handling Editor: Prof D Bryce

Keywords:
Solid-state NMR
Ultrahigh-field
1.5 GHz
^{13}C
Linewidth
Fungi
Carbohydrate

ABSTRACT

Ultrahigh-field solid-state NMR in the GHz frequency range has opened new frontiers for probing complex, heterogeneous biological systems with unprecedented spectral resolution. Here, we demonstrate the advantages of a 1.5 GHz (35.2 T) NMR spectrometer for cellular solid-state NMR by quantitatively assessing ^{13}C linewidth improvements in intact, living fungal cells of *Aspergillus fumigatus*. High-quality 2D ^{13}C-^{13}C correlation spectra were acquired within 2-5 h, showing consistent linewidth narrowing of 0.05-0.15 ppm under idealized conditions and exceeding 0.2 ppm under realistic, power-limited running time constraints relative to 800 MHz. The resolution gains are especially pronounced for overlapped and inhomogeneously broadened resonances in multidimensional correlation experiments and are most significant in power-demanding recoupling experiments where acquisition times must be shortened. These improvements enable the resolution of extensive previously inaccessible spectral multiplicity and structural polymorphism in cellular carbohydrates such as chitin and α-1,3-glucan, while substantially reducing experimental time relative to lower-field approaches. These results illustrate the potential advantages of ultrahigh-field solid-state NMR for improving spectral resolution in complex cellular materials and emphasize the importance of continued development of computational and analytical approaches to effectively interpret the increasingly information-rich spectra obtained at these fields.

1. Introduction

Solid-state NMR spectroscopy has long been an essential tool for probing the atomic-level structure and dynamics of complex materials and biomolecules. Among the most significant recent advances is the development of ultrahigh magnetic fields in the GHz frequency range [1]. The availability of these magnets, recently from 1.2 GHz commercial NMR systems (28.2 T) to the 1.5 GHz (35.2 T) world-record field achieved using series-connected hybrid (SCH) magnet technology from 2018, represents not merely an incremental improvement but opens entirely new frontiers for understanding complex matter at the atomic scale [2]. Access to these higher fields provides advantages, including enhanced sensitivity, greatly improved spectral resolution, and the ability to resolve crowded spectral regions that remain intractable at conventional fields [3]. Early successes were achieved with quadrupolar nuclei, for which ultrahigh magnetic fields reduce the second-order quadrupolar broadening, which scales inversely with magnetic field strength, while increasing spectral dispersion and sensitivity critical for low gamma, low abundance nuclei, and have more recently extended to conventional proton-detected biomolecular systems [4–6].

One of the most exciting applications is in materials science and catalysis, where access to GHz magnetic fields provides unprecedented insight into disordered phases and subtle structural features that govern functional properties [2,7]. Access to 1.2 GHz and 1.5 GHz spectrometers with fast magic-angle spinning (MAS) has resolved distinct surface proton and ^{27}Al signatures in zeolites and γ-Al_2O_3, directly identifying

This article is part of a special issue entitled: ssNMR above 1 GHz and beyond published in Solid State Nuclear Magnetic Resonance.

* Corresponding author. Department of Chemistry, Michigan State University, East Lansing, MI, USA.
** Corresponding author.
E-mail addresses: Malitha.Dickwella@nrel.gov (M.C. Dickwella Widanage), wangtuo1@msu.edu (T. Wang).
[1] These authors contributed equally.
[2] Present address: Department of Chemistry and Biochemistry, California State University, Eastbay, CA, USA.

https://doi.org/10.1016/j.ssnmr.2026.102075
Received 12 February 2026; Received in revised form 11 March 2026; Accepted 18 March 2026
Available online 19 March 2026

long-hypothesized Al(V) sites and revealing active-site environments central to Brønsted and Lewis acidity [8]. ^{17}O-based 2D correlation experiments at 1.5 GHz NMR further enabled mapping of the oxygen species distribution in this catalyst by distinguishing surface hydroxyls from subsurface oxygens and revealing their spatial proximities to each other and to bulk oxygens [9]. In addition, ^{67}Zn solid-state NMR at 1.5 GHz revealed structure-property relationships relevant to MOF glass formation by showing that melt quenching transforms crystalline ZIFs with two distinct Zn sites into glasses with a single tetrahedral Zn environment exhibiting pronounced short-range disorder, largely independent of ligand chemistry [10].

Ultrahigh-field solid-state NMR has enabled advances across biological systems, from early successes with quadrupolar nuclei to proton-detected ultrafast MAS experiments. ^{17}O-involved multidimensional correlation experiments at 1.5 GHz demonstrated that quadrupolar oxygen nuclei can be resolved with site- and residue-specificity, enabling direct measurement of local structure and hydrogen-bonding interactions in amino acids and a di-peptide [11,12]. ^{17}O NMR at 1.5 GHz directly revealed stable, site-specific hydrogen bonding between a confined water wire and select backbone carbonyls in the gramicidin A ion channel, providing insight into water-protein interactions that govern channel function [13]. Proton-detected experiments at 1.2 GHz with 100-160 kHz MAS yielded markedly sharpened multidimensional spectra of membrane proteins such as M2, VDAC, and Opa60, with superlinear resolution gains that enabled cleaner resonance assignments, higher-dimensional (3D/4D) experiments, and resolution of ~2-2.5-fold more signals [14]. At the same field, ultrafast MAS enabled unprecedented side-chain proton assignments in the HBV Cp149 viral capsid, resolving 61% of aliphatic protons, an achievement unattainable at conventional fields, while systematic comparisons across proteins, fibrils, and large assemblies confirm substantial resolution gains at 1.2 GHz [3,15].

Here, we focus on the implications of ultrahigh magnetic fields for solid-state NMR studies of intact, heterogeneous cellular systems, where spectral congestion and inhomogeneous broadening present long-standing challenges. Using living *Aspergillus fumigatus* cells as a model, which is a pathogenic filamentous fungus that has shown exceptionally well-resolved NMR spectra in recent studies [16,17], we show that access to a 1.5 GHz spectrometer fundamentally alters the resolvable information content of ^{13}C-based correlation spectra, particularly for densely packed carbohydrate networks in the fungal cell wall. The enhanced resolution preferentially benefits overlapped and structurally heterogeneous resonances and is most impactful in power-demanding recoupling experiments where acquisition times must be constrained. These capabilities expose a level of structural polymorphism in carbohydrates such as chitin and α-1,3-glucan that has not been accessible at lower fields, while also motivating the development of new analytical and computational strategies to interpret the greatly expanded spectral complexity enabled by ultrahigh-field NMR.

2. Results and discussion

Before presenting and discussing the effects of magnetic field strength on the spectral resolution of intact, living *Aspergillus fumigatus* cells, it is useful to first categorize the various sources of line broadening and their field dependence in 1D and 2D solid-state NMR spectra. In solids, spectral resolution is determined by the interplay between homogeneous and inhomogeneous broadening mechanisms [18]. The most fundamental contribution comes from T_2 relaxation, referring to the irreversible decay of phase coherence driven by stochastic molecular motions. The exponential decay of the free induction decay (FID) signal leads to Lorentzian broadening with fullwidth at half height of $1/(\pi T_2)$. For abundant or isotopically enriched nuclei, additional major sources of homogeneous broadening include residual dipolar couplings under magic-angle spinning (MAS) and homonuclear *J*-couplings. Except for a few specialized experiments capable of selecting an individual state of an isolated spin pair, signal decay arising from homonuclear couplings is generally not refocusable using spin echoes or coherence-transfer echoes.

Homogeneous broadening expressed in units of ppm is generally inversely proportional to the magnetic field strength, assuming field-independent T_2 and spin-spin couplings [19]. A major exception occurs when chemical shift anisotropy (CSA) or chemical exchange contributes significantly to incoherent relaxation, as is often observed for dynamic or mobile species [20]. In such cases, the contribution to T_2 relaxation scales with the square of the magnetic field strength (B_0^2) [21]. For example, dynamic aromatic or carbonyl carbons undergoing random motional fluctuations of the CSA tensor are expected to exhibit linewidth broadening in ppm at higher magnetic fields. For the rigid carbohydrate signals investigated in this study, however, these dynamic contributions are negligible. As a result, the suppression of *J*-couplings and dipolar interactions should remain the dominant factor governing resolution enhancement, and higher magnetic fields lead to narrowing of the homogeneous component of the linewidth in ppm. A prominent example is the enhancement of proton resolution achieved at high magnetic fields under fast MAS, where residual higher-order broadening from strong homonuclear dipolar interactions is often a dominant source of linewidth broadening in the direct ^{1}H dimension [22,23]. In multidimensional experiments, this line narrowing applies to all indirect dimensions, depending on the T_2 relaxation and homonuclear couplings of the observed spins.

The second major category of line broadening, often referred to as inhomogeneous broadening, originates from early NMR studies in which magnetic field inhomogeneity was the primary limiting factor for spectral resolution. Inhomogeneous broadening is constant in ppm and scales linearly with magnetic field strength in frequency units. While magnetic field inhomogeneity from modern superconducting magnets has been reduced to the ppb level, significant inhomogeneous broadening in solid-state NMR arises from the sample and its environment. These contributions include variations in magnetic susceptibility in the surroundings, anisotropic bulk magnetic susceptibility of the sample itself, which is not averaged by MAS, and, most importantly for solids, distributions of chemical shifts and local magnetic fields arising from structural and environmental disorder.

For 1D spectra, higher magnetic fields do not reduce inhomogeneous broadening and therefore do not directly improve spectral resolution. The situation differs, however, for multidimensional correlation NMR experiments. In these experiments, chemical shift and local field distributions along different dimensions can become correlated. Such correlations lead to partial signal refocusing in the form of coherence-transfer echoes [19], resulting in tilted peak shapes with slopes determined by the coherence-order ratios, for example a slope of 1 (corresponding to an approximately 45° ridge) in 2D ^{13}C-^{13}C correlation spectra. In principle, 1D slices extracted from these 2D spectra reflect primarily the homogeneous contribution to the linewidth, such that higher magnetic fields can improve apparent spectral resolution, as discussed above.

The extent of resolution enhancement in two- and multidimensional spectra depends on several additional factors. Short-range structural disorder can give rise to uncorrelated chemical shift distributions that are not refocused in multidimensional correlation experiments. This behavior has been clearly demonstrated in the 2D ^{13}C-^{13}C peak shape of cellulose [24] and likely applies to *A. fumigatus* cells as well. Furthermore, line shapes arising from different broadening mechanisms may coexist and mix in 2D spectra, for example star-like features associated with Lorentzian T_2 broadening and more rounded features associated with Gaussian decay. Data processing procedures introduce additional complexity: window functions and time-domain truncation, particularly in indirect dimensions, further influence the observed line shapes. All of these factors are taken into account in the comparison of spectra acquired at 1.5 GHz and 800 MHz and in the discussion of high-field effects on the spectral resolution of *A. fumigatus* cells.

2.1. Linewidth analysis: 0.05-0.15 ppm ^{13}C linewidth improvement at 1.5 GHz versus 800 MHz

Intact and living cells of ^{13}C,^{15}N-labeled *A. fumigatus* were packed into a 2.0-mm MAS rotor with a sample volume of 10 μL using a home-built 2.0 mm HCN probe. Measurements performed on a 1.5 GHz NMR spectrometer enabled acquisition of a high-resolution 2D^{13}C-^{13}C correlation spectrum within 4.6 h (Fig. 1A). The 2D spectrum was acquired in multiple blocks then summed, with each block spanning 0.3-0.7 h considering that the SCH magnet is running in parallel with other magnets at the facility and unpredictable incoming power conditions. To ensure spectral consistency across these acquisition blocks, magnetic field stability was monitored by periodically inspecting the positions of representative peaks in the spectra, particularly along the indirect dimension. No significant field drift was observed within individual acquisition blocks. The individual 2D datasets were referenced using 1D spectra recorded between blocks to ensure consistent chemical shift calibration prior to summing the data. A recycle delay of 1.8 s was used between scans to allow sufficient longitudinal relaxation recovery.

Owing to the use of an ultrahigh magnetic field and moderately fast MAS of 24 kHz, which are required to reduce spinning sidebands at high field, a long DARR mixing time of 200 ms was necessary to establish intramolecular cross peaks. This performance is comparable to that obtained using shorter periods (50-53 ms) of DARR/CORD mixing on a conventional 800 MHz spectrometer operating at slower MAS rates of 12-14 kHz. At faster MAS, longer DARR mixing times are required to achieve comparable recoupling efficiency, which is the primary reason why a 200 ms DARR mixing time was used at 1.5 GHz. Under these conditions, the resulting spectra show cross-peak patterns comparable to those reported previously at 800 MHz, including the complete set of intramolecular correlations within α- and β-glucans as well as weaker cross peaks from chitin. In addition, the different MAS rates were chosen such that the first spinning sidebands appear at similar positions in ppm units at both fields, thereby maintaining a comparable overall spectral pattern.

Standard acquisition parameters commonly used on high-field spectrometers were employed, with acquisition times of 18 ms for the direct dimension and 8 ms for the indirect dimension. The latter was chosen to minimize the total experimental time while avoiding significant artifacts arising from truncation of the indirect-dimension FID. Despite the small sample volume and the well-hydrated nature of the whole-cell material, high-quality cross sections were obtained with an accumulated total of only 26 scans, exhibiting excellent resolution and signal-to-noise ratios of 4-28 (Fig. 1B).

Direct comparison of linewidths between the 1.5 GHz and 800 MHz datasets is nontrivial, as digital (FID) resolution must also be considered. According to Nyquist theorem, the digital resolution (*res*, in Hz/point) in NMR is dictated by the acquisition time (*aq,* in seconds), the spectral width (*sw,* in Hz), and the number of acquired points (*np*) as follows:

$$res(Hz) = \frac{1}{aq} = \frac{2 \cdot sw(Hz)}{np}$$

In multidimensional NMR, this applies independently to both the indirect (*aq1*) and direct (*aq2*) dimensions. While the resolution in Hz depends strictly on the acquisition time, the resolution in ppm, which is the critical metric for comparing spectral features, is inversely proportional to the magnetic field strength:

$$res(ppm) = \frac{res(Hz)}{\upsilon_0}$$

Where υ_0 is the Larmour frequency in MHz. Consequently, at higher magnetic fields, a fixed acquisition time (*aq*) results in a finer digital resolution in ppm, necessitating longer acquisition times at lower fields to achieve a matching sampling density. For example, under identical spectral width settings, acquisition times of 10 ms (aq1) and 18 ms (aq2) at 1.5 GHz correspond to 18.75 ms and 33.75 ms, respectively, on an 800 MHz spectrometer to achieve the same FID resolution in units of ppm. However, an aq2 as long as 33.75 ms on a natively hydrated cellular sample poses a substantial risk of probe performance deterioration due to the prolonged application of high-power decoupling. In addition, an aq1 of 18.75 ms would require a very large number of indirect-dimension increments, resulting in long experimental times for the 2D experiment.

In principle, the optimal acquisition time is set by T_2 relaxation; in practice, however, the useable acquisition window for these fully hydrated cellular samples is also limited by radiofrequency power deposition during continuous high-power ^1H decoupling, particularly in experiments that include additional high-power elements such as PAR.

The reported 26 scans correspond to the total number of scans

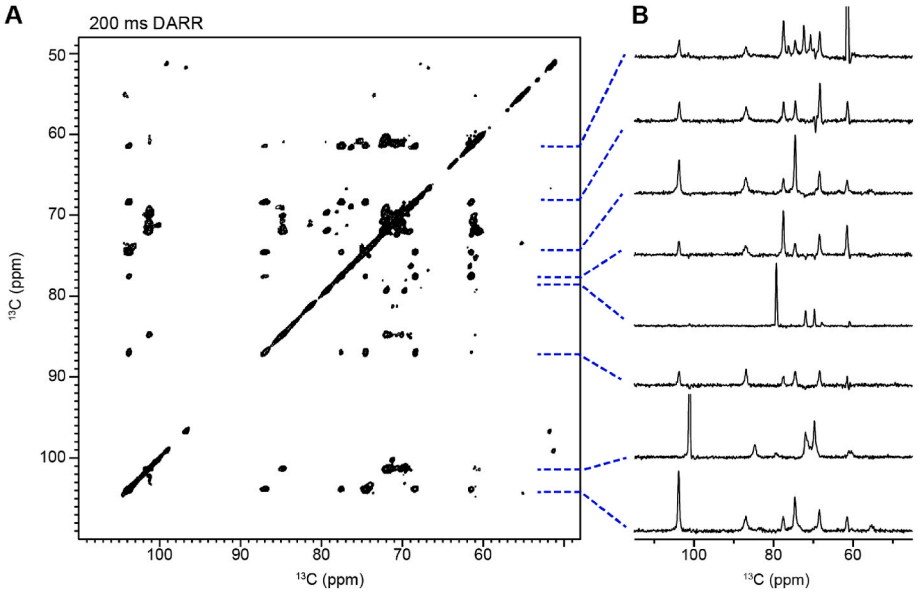

Fig. 1. ^{13}C-^{13}C DARR spectrum of 10 μL of living *A. fumigatus* cells at 1.5 GHz within 4.6 h. (**A**) Carbohydrate region of 200 ms DARR spectra. (**B**) Representative cross sections showing high signal-to-noise for key carbohydrate carbon sites. The spectra were collected within 4.6 h with 26 scans on 10 μL of living cells. Each block takes 0.3-0.7 h. The key parameters are aq1 = 8 ms, aq2 = 18 ms. The spectra were processed with QSINE window function with SSB of 3.5.

accumulated across several blocks of 2D experiments, rather than scans acquired for a single 2D spectrum. Each individual spectrum was recorded with only 2-4 scans, requiring approximately 0.3-0.7 h per block to accommodate the limited magnetic field stability during the experiment. Under these constraints, the flexibility to redistribute experimental time between the number of scans and the acquisition window in the indirect dimension is limited. In addition, the spectral width was already set to the minimum value required to cover the full spectral range of the signals, leaving little room to further modify the sampling increments.

To allow a fair and practical comparison, we therefore adopted a compromise acquisition scheme. The 1.5 GHz 2D spectrum was reprocessed using truncated acquisition times of aq1 = 7.5 ms and aq2 = 15 ms, yielding an FID resolution equivalent to that of a 2D spectrum acquired at 800 MHz with aq1 = 14 ms and aq2 = 28 ms, respectively (Fig. 2A, middle vs. bottom panels). Under these matched resolution conditions, the 1.5 GHz spectra exhibited a moderate improvement over the 800 MHz data, manifested as narrower linewidths. Quantitative analysis of the full width at half maximum (FWHM) revealed reductions from 0.51 ppm to 0.46 ppm for the resolved (60, 101) ppm cross peak, from 0.42 ppm to 0.35 ppm for (85, 70) ppm, and from 0.50 ppm to 0.27 ppm for (101, 61) ppm. These cross peaks correspond to the C6-C1, C3-C4, and C1-C6 correlations, respectively, of α-1,3-glucan in *A. fumigatus* cell walls (Fig. 2B, middle vs. bottom panels).

For these well-resolved cross peaks, only a slight linewidth improvement of 0.01-0.02 ppm was observed when the full 1.5 GHz FID was retained, compared with the truncated FID processing (Fig. 2B, top vs. middle panels). In contrast, the improvement was more pronounced for overlapped peaks. For example, the (104, 87 ppm) cross peak, corresponding to the C1-C3 correlation in the β-glucan matrix, exhibited a linewidth narrowing of 0.1 ppm when comparing the 800 MHz data to the resolution-matched 1.5 GHz spectrum, with a further reduction observed in the untruncated 1.5 GHz spectrum. This cross peak is intrinsically broadened by inhomogeneous contributions arising from both the coexistence of 1,3-linked linear domains and 1,3,6-linked branching units within the β-1,3-glucan polymeric network, as well as the presence of multiple structural forms of β-1,3-glucans. These include triple-helical conformations in the matrix and flattened conformations when β-1,3-glucans are folded onto the surfaces of chitin microfibrils.

Analysis of peak counts as a function of FWHM linewidth further shows that, under Squared Sine-bell (QSINE) window-function processing with a sinebell shift (SSB) of 3.0, most peaks in the 800 MHz spectrum cluster within the 0.45-0.60 ppm range (Fig. 3A; Fig. S1). In contrast, this distribution shifts to 0.40-0.55 ppm in the 1.5 GHz spectra, regardless of whether FID truncation is applied. In addition, the 1.5 GHz spectrum exhibits very sharp peaks in the 0.25-0.40 ppm range, whereas the 800 MHz spectrum contains only a single peak in the 0.35-0.40 ppm range and none at narrower linewidths. The 800 MHz spectrum also

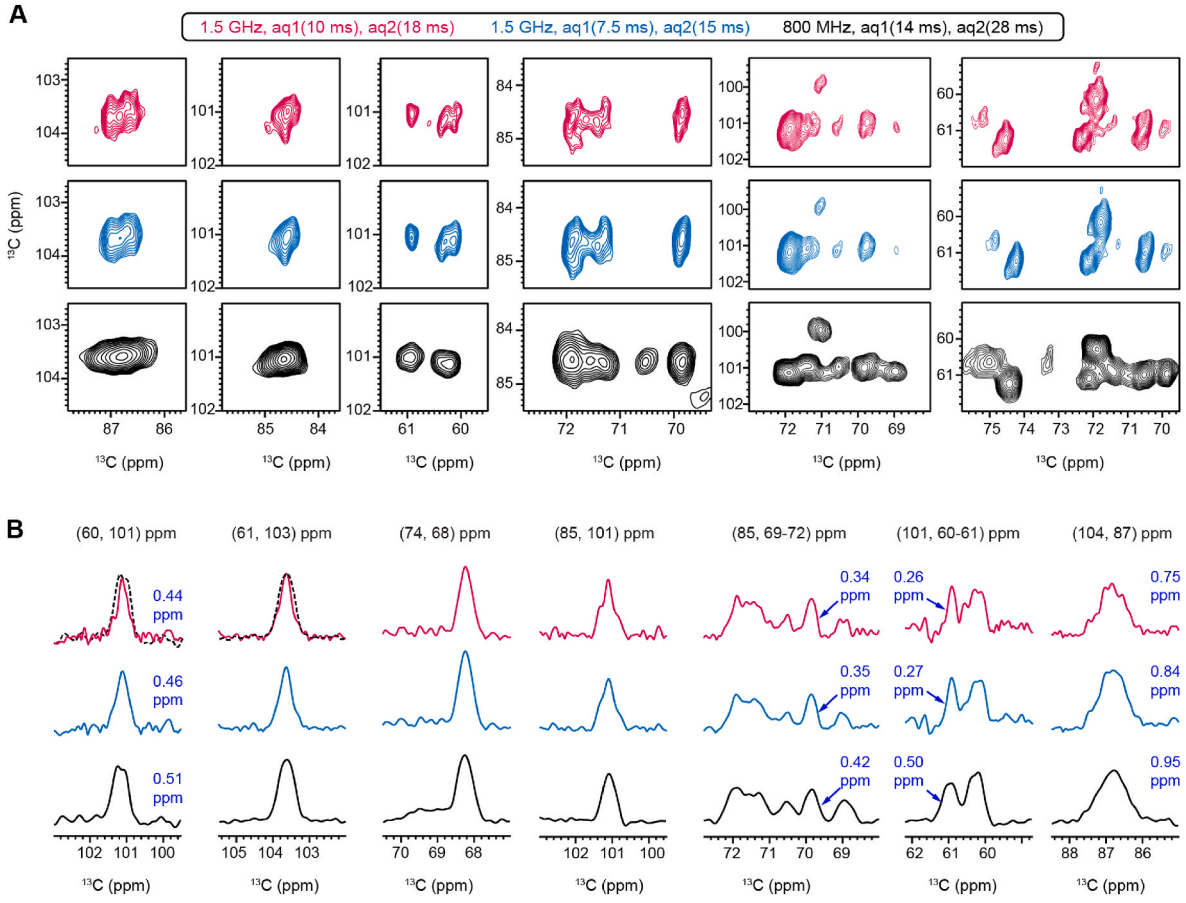

Fig. 2. Linewidth analysis of 2D DARR/CORD spectra acquired with extremely long acquisition. (**A**) Zoomed-in views of representative carbohydrate regions from a 200 ms DARR spectrum recorded at 1.5 GHz with 24 kHz MAS (top and middle panels) and a 53 ms CORD spectrum recorded at 800 MHz with 13.5 kHz MAS (black; bottom panel). All spectra were processed using a QSINE window function with an SSB of 3.0. The 800 MHz data was processed with its full FID with aq1 extending to 14 ms and aq2 extending to 28 ms. The 1.5 GHz data were analyzed using two processing schemes: full FIDs with acquisition times of aq1 = 10 ms and aq2 = 18 ms (magenta; top), and truncated FIDs with aq1 = 7.5 ms and aq2 = 15 ms (blue; middle). (**B**) Representative cross sections extracted for comparison between the 1.5 GHz and 800 MHz datasets, using the same processing parameters and color coding as in panel-A. The FWHM linewidths are indicated in blue for selected cross sections. In the first two panels, the 800 MHz data are overlaid as black dashed lines for direct comparison with the 1.5 GHz data shown in magenta. (For interpretation of the references to color in this figure legend, the reader is referred to the Web version of this article.)

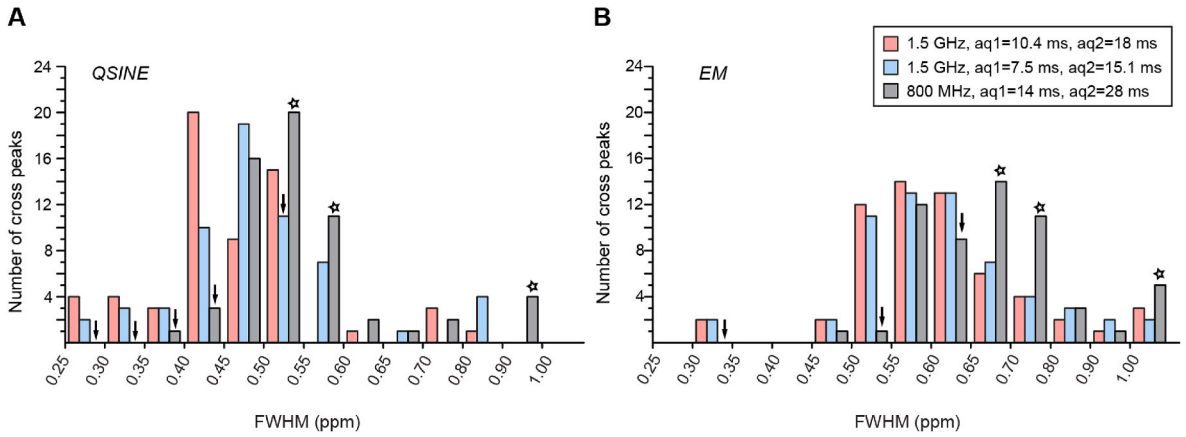

Fig. 3. FWHM Linewidths of 2D DARR/CORD spectra acquired with extremely long acquisition. (**A**) Peak count of carbohydrate signals from a 200 ms DARR spectrum recorded at 1.5 GHz with 24 kHz MAS and a 53 ms CORD spectrum recorded at 800 MHz with 13.5 kHz MAS. All spectra were processed using a QSINE window function with an SSB of 3.0. The 800 MHz data was processed with its full FID with aq1 extending to 14 ms and aq2 extending to 28 ms (grey bars). The 1.5 GHz data were analyzed using two processing schemes: full FIDs with acquisition times of aq1 = 10 ms and aq2 = 18 ms (red bars), and truncated FIDs with aq1 = 7.5 ms and aq2 = 15 ms (blue bars). Black arrows indicate a substantial decline in the peak count within a given linewidth range, while open asterisks indicate an increase in the peak count in the 800 MHz data compared to the 1.5 GHz data. (**B**) FWHM distributions of spectra processed using an exponential multiplication (EM) window function with a line broadening of 0.05 ppm, corresponding to an LB of 18.75 Hz for the 1.5 GHz data and 10 Hz for the 800 MHz data. (For interpretation of the references to color in this figure legend, the reader is referred to the Web version of this article.)

shows several very broad peaks in the 0.9-1.0 ppm range, attributable to inhomogeneous broadening as discussed above. Within the 1.5 GHz datasets, retaining the full FID has a noticeable effect, approximately doubling the number of sharp peaks in the 0.40-0.45 ppm range from 10 to 20.

When the window function was changed to exponential multiplication (EM) with a line broadening of 0.05 ppm applied consistently to all three datasets, a similar trend was observed, although all FWHM values were larger than those obtained using QSINE processing (Fig. 3B). Under EM processing, most peaks in the 800 MHz spectrum fall within the 0.55-0.80 ppm range, whereas this distribution shifts to 0.50-0.65 ppm for the 1.5 GHz datasets. Thus, regardless of the choice of window function or the application of FID truncation, a consistent narrowing of at least 0.05-0.15 ppm in the ^{13}C linewidth is observed for most peaks at 1.5 GHz compared with 800 MHz.

This observed subtle narrowing of ^{13}C linewidths under matched digital acquisition and processing conditions is likely real and driven primarily by the favorable field-scaling of coherent homogeneous broadening mechanisms including homonuclear ^{13}C-^{13}C *J*-couplings (~35-55 Hz) and truncation of residual dipolar couplings [18]. However, we note that this improvement may also be partially attributed to the experimental differences mandated by the hardware, such as the slightly faster MAS rate used at 1.5 GHz. While faster MAS contributes to the averaging of anisotropic interactions, the observation that the narrowing is subtle but meaningful under acquisition-matched conditions suggests that the resolution is approaching the inhomogeneous limit defined by the structural disorder of the cell wall.

2.2. Realistic condition: significant improvement of ^{13}C linewidth at 1.5 GHz versus 800 MHz

The 800 MHz dataset used in the previous section required extremely long acquisition times, with t_2 (F2) acquisition of 28 ms under continuous high-power ^{1}H decoupling. Such conditions are particularly challenging for fully hydrated, living cellular samples, as they substantially increase the risk of arcing and long-term probe performance degradation, making this approach impractical for routine use in most NMR facilities. In addition, the long t_1 evolution time of 14 ms necessitates a large number of indirect-dimension increments, leading to prohibitively long total experimental times for acquiring the 2D spectra and increasing the risk of significant magnetic field drift, particularly at high fields [3].

To enable a more practical comparison, the DARR and CORD spectra were therefore acquired at both 1.5 GHz and 800 MHz using identical acquisition parameters (aq1 = 10 ms and aq2 = 18 ms), which are typical values for biomolecular solid-state NMR experiments [25]. Under these laboratory-affordable conditions, the resolution enhancement afforded by the ultrahigh magnetic field is even more pronounced. The 1.5 GHz spectra resolve fine spectral features that are not discernible in the corresponding 800 MHz data (Fig. 4A) and exhibit substantial linewidth improvements for multiple resolved peaks, with FWHM values reduced from 0.51 ppm at 800 MHz to 0.29-0.35 ppm at 1.5 GHz (Fig. 4B), with 0.2 ppm improvement.

FWHM linewidth analysis further reveals that the 1.5 GHz spectrum contains 11 peaks in the 0.25–0.40 ppm range, which are entirely absent in the 800 MHz spectrum. In contrast, the 800 MHz spectrum exhibits seven peaks in the broader 0.55-0.60 ppm range that are not observed among the resolved peaks in the 1.5 GHz data. Peaks with FWHM values exceeding this range primarily originate from signals containing overlapping components, for which the 1.5 GHz data begin to resolve finer features but do not fully separate them into distinct peaks, whereas the 800 MHz data display these signals as a single broadened resonance.

The limitation on FID length becomes even more severe for pulse sequences that incorporate additional high-power blocks, such as proton-assisted recoupling (PAR), in which the ^{1}H and ^{13}C channels are simultaneously irradiated for 10-20 ms [26,27]. To safely perform these high-power experiments, we limited the acquisition times to aq1 of 6-8 ms and aq2 of 16-17 ms. Even when slightly longer acquisition times were used for the 800 MHz experiments compared to those at 1.5 GHz, the 800 MHz spectra remained substantially broader than the corresponding 1.5 GHz spectra (Fig. 4D; Fig. S2). Consequently, the resolution improvement afforded by the ultrahigh magnetic field becomes even more pronounced when acquisition times must be restricted for power-demanding experiments.

2.3. Ultrahigh magnetic fields require reconsideration of data analysis strategies

The unparalleled resolution afforded by the 1.5 GHz NMR spectrometer enables the resolution of structural polymorphism in cellular carbohydrates at an unprecedented level. Taking chitin as an example, this polymer is chemically simple, consisting of β-1,4-linked GlcNAc

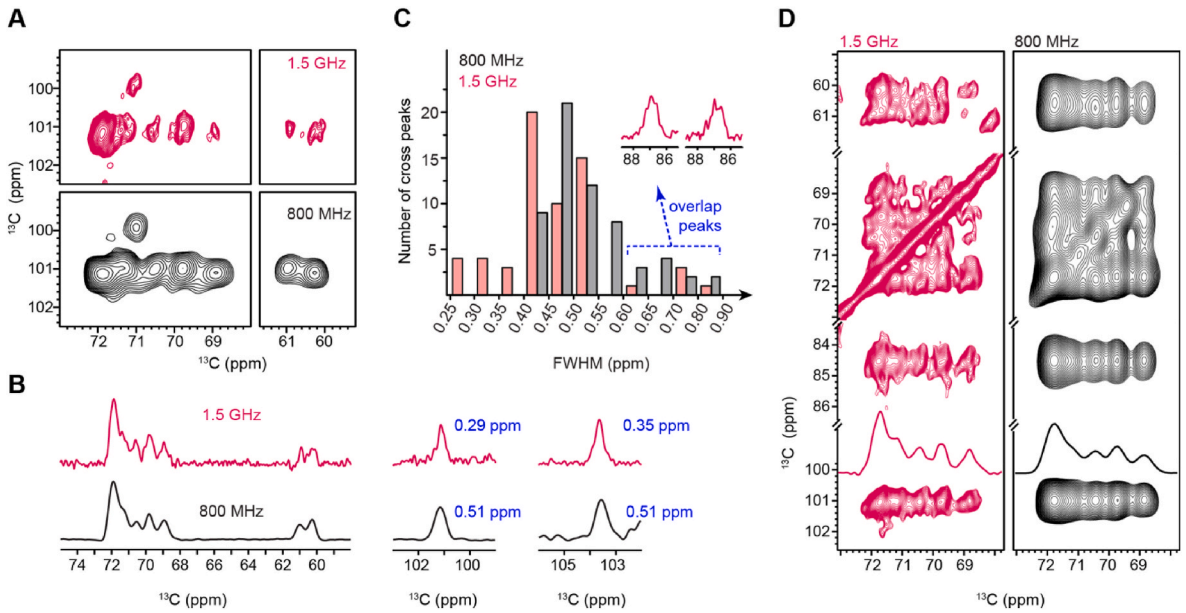

Fig. 4. Ultrahigh-field improves resolution in spectra acquired with realistic acquisition conditions. (**A**) Representative carbohydrate panel from 200-ms DARR spectrum collected on 1.5 GHz spectrometer (magenta) with 24 kHz, and 53-ms CORD spectrum collected on 800 MHz spectrometer (black) with 13.5 kHz MAS. The aq1 was 10 ms for 800 MHz data and 18 ms for 1.5 GHz data, while aq2 was 18 ms for 800 MHz data and 10 ms for 1.5 GHz data. Both spectra were processed using QSINE with SSB of 4.0. (**B**) Representative cross sections extracted from the two 2D PAR spectra. FWHM linewidths are labeled in blue. (**C**) Number of cross peaks falling into different linewidth ranges from the spectra collected on two different magnetic fields under realistic acquisition conditions outlined in panel-A. (**D**) Comparison of 2D 15-ms PAR spectra between 1.5 GHz and 800 MHz 15 ms PAR spectra. The aq1 was 8 ms for 800 MHz data and 6 ms for 1.5 GHz data, while aq2 was 17 ms for 800 MHz data and 16 ms for 1.5 GHz data. Both spectra were processed using QSINE with SSB of 3.0. (For interpretation of the references to color in this figure legend, the reader is referred to the Web version of this article.)

units forming chains that are predominantly antiparallel and associated through extensive hydrogen bonding. Despite this chemical simplicity, the resulting ^{13}C-^{13}C 2D spectrum was remarkably complex, with more than 20 distinct fine features resolved within each small spectral region (Fig. 5, left). High structural complexity was also evident in the $_{H}$N-C correlations (Fig. 5, bottom), where 16-22 distinct features were resolved in the $_{H}$N-C1 (C1: 103-105 ppm) and $_{H}$N-C4 (C4: 83-85 ppm) correlation regions. This level of complexity exceeds that previously accessible using ^{13}C-based solid-state NMR, in which typically only 4-7 chitin signal forms in each fungus could be resolved (typically four forms for the *A. fumigatus* mycelia used in the present study) [16,28,29], as well as ^{1}H-detected experiments, such as the 3D hcoCH3coNH sequence, which, although more sensitive to hydrogen-bonding interactions, resolve maximally 13-14 features [30].

Importantly, each of the ultrahigh-field experiments (the 2D^{13}C-^{13}C PAR and the 2D^{15}N-^{13}C correlation) was completed within approximately 2 h. This represents a substantial reduction in experimental time compared with 2D^{13}C-^{13}C/^{15}N experiments on lower fields, which also resolve far fewer features, or 3D ^{1}H-detected hcoCH3coNH experiment on an 800 MHz NMR that achieve slightly less resolution and require 55 h of experimental time [30]. At the same time, ^{1}H-detected approaches have demonstrated tremendous power for biomolecular systems and are increasingly being extended to cellular and carbohydrate-rich materials [31]. Continued methodological developments in this area are expected to further enhance the ability of ^{1}H detection to resolve fine structural features within practical experimental time.

Similarly, α-1,3-glucan also exhibits high spectral multiplicity, despite being a structurally simple polymer composed of glucose units linked exclusively through α-1,3 glycosidic bonds [32,33]. For example, four to five distinct horizontal lines (ω_1) of cross-peaks were resolved in the C6 region at 60-61 ppm, in addition to those resolvable from the vertical lines (ω_2), revealing a large number of fine spectral features. α-1, 3-glucan is known to function as a buffering and adhesive carbohydrate that associates with a wide range of polysaccharides across the cell wall. The new level of structural polymorphism enabled by ultrahigh-field provides a unique opportunity to elucidate the relationship between its structural heterogeneity and functional multiplicity.

A key challenge that remains, however, is how to translate this wealth of ultrahigh-field NMR information into meaningful structural insight. We anticipate that applying high-field NMR to other carbohydrate-rich and cellular samples, such as bacteria, plants, and the human extracellular matrix, will encounter similar barriers to those observed here for fungi [34–38]. Addressing this challenge will require the development of semi-automated algorithms for peak picking, pattern recognition, and resonance assignment, increasingly informed by machine learning and AI approaches trained on an expanding body of reference data on cellular carbohydrates [39–42]. With the rapid data acquisition enabled by sensitivity gains at ultrahigh fields, and the greatly increased number of resolvable peaks arising from improved spectral resolution under realistic experimental conditions, such computational and analytical advances are becoming increasingly essential.

3. Conclusions

The results presented here illustrate how ultrahigh magnetic fields reshape the practical limits of solid-state NMR for complex, heterogeneous biological samples, particularly under conditions where experimental constraints traditionally compromise resolution. By enabling meaningful linewidth reductions under practical experimental conditions where acquisition times are constrained by radiofrequency power deposition, 1.5 GHz operation shifts the balance between feasibility and information content in favor of high-resolution cellular spectroscopy. The ability to disentangle fine spectral features in structurally diverse carbohydrate networks highlights the potential of ultrahigh-field NMR to address long-standing questions related to molecular heterogeneity and functional organization in native biological environments. Looking forward, continued progress in ultrafast MAS experimental design and

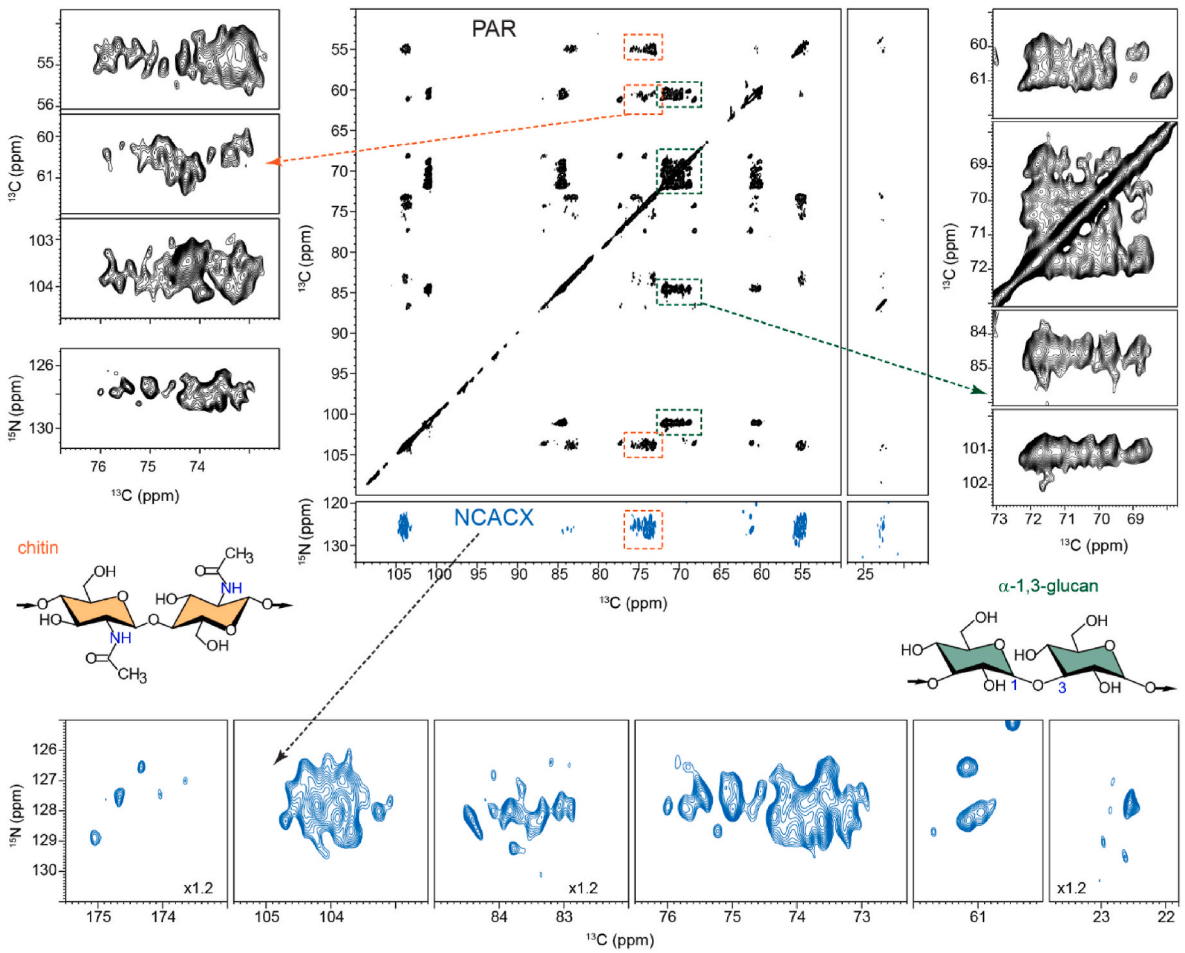

Fig. 5. Ultrahigh-field solid-state NMR provides high resolution in polymorphic polymers. A 2D^{13}C-^{13}C 15 ms PAR spectrum (black) and a 2D^{15}N-^{13}C correlation spectrum acquired using the NCACX sequence (blue) are shown in the center of the figure. The PAR spectrum was completed within 2 h using 8 scans, while the ^{15}N-^{13}C 2D spectrum was completed in 2.1 h using 160 scans. Representative regions of chitin are highlighted with orange dashed boxes, magnified, and shown on the left. Representative regions of α-1,3-glucan signals are highlighted with green dashed boxes, magnified, and shown on the right. The ^{15}N-^{13}C correlation cross peaks of chitin are further magnified and shown at the bottom. (For interpretation of the references to color in this figure legend, the reader is referred to the Web version of this article.)

magnet stability is expected to further extend these gains. Together, these advances point toward a future in which ultrahigh-field solid-state NMR becomes an enabling technology for routinely accessing atomic-level detail in systems of previously prohibitive complexity.

4. Material and methods

4.1. Preparation of uniformly ^{13}C,^{15}N-labeled fungal materials

Aspergillus fumigatus (strain Af293) was cultured in YPD media at 30 °C for seven days [43]. For isotopic labeling, liquid cultures were grown in modified minimal medium containing ^{13}C-glucose (10.0 g/L) and ^{15}N-sodium nitrate (6.0 g/L), adjusted to pH 6.5. Cultures (100 mL) were incubated in 250 mL flasks at 210 rpm and 30 °C. Mycelia were collected by centrifugation (7000×*g*, 20 min), washed with 10 mM PBS (pH 7.4), and packed for NMR: 30 mg into 3.2 mm and 10 mg into 2.0 mm MAS rotors for solid-state NMR, preserving native hydration.

4.2. Solid-state NMR experiments

All ssNMR experiments were performed on a series-connected hybrid magnet operating at 1.5 GHz (35.2 T) and on a Bruker Avance 800 MHz (18.8 T) spectrometer [2]. Experiments were conducted at 24 kHz using a home-built 2.0 mm HCN probe on the 1.5 GHz NMR, and at 13.5 kHz MAS using a 3.2 mm HCN probe on the 800 MHz. All experiments were carried out at 294 K. ^{13}C shifts were externally referenced to the TMS scale by calibrating adamantane CH_2 peak to 38.48 ppm. ^{15}N chemical shifts were referenced to the liquid ammonia scale by calibrating the methionine amide peak of N-formyl-Met-Leu-Phe-OH to 127.88 ppm. Typical field strengths of radiofrequency pulses were 62.5 kHz for ^{1}H hard pulses and 50-62.5 kHz for ^{13}C. ^{1}H-decoupling was achieved using the SPINAL-64 sequence, with field strengths of 80-100 kHz, which is a standard setup sufficient to ensure sharp lines for hydrated biological samples. Alternative low-power heteronuclear decoupling schemes have been developed for MAS NMR, including XiX-type decoupling and other reduced-power approaches at high spinning frequencies, which may provide opportunities to mitigate RF power deposition in future ultrahigh-field experiments [44,45].

Five 2D^{13}C-^{13}C correlation experiments were conducted on both spectrometers, including 53 ms CORD spectra acquired at 800 MHz with acquisition times of 10 ms in the indirect dimension and 18 ms in the direct dimension, as well as with 14 ms and 28 ms, respectively; a 200 ms DARR spectrum acquired at 1.5 GHz with acquisition times of 10.4 ms and 18 ms; and 15 ms PAR spectra acquired at 800 MHz and 1.5 GHz with acquisition times of 8 ms and 17 ms, and 6 ms and 16 ms, respectively [25,26]. All spectra were subjected to different window-function multiplications and, where indicated, processed with truncated effective acquisition times, as described throughout the

maintext, to support direct comparison across magnetic fields. The ^{1}H and ^{13}C irradiations during PAR period were 53 kHz and 56 kHz, respectively. In addition, a ^{15}N-^{13}C correlation spectrum was recorded using the NCACX pulse sequence on the 1.5 GHz to record chitin $_{H}N$-C correlations [46,47].

Declaration of competing interest

The authors declare that they have no known competing financial interests or personal relationships that could have appeared to influence the work reported in this paper.

Acknowledgment

This work was primarily supported by National Science Foundation (NSF) under grant number MCB-2517270 and National Institutes of Health (NIH) grant R01AI173270. The National High Magnetic Field Laboratory is supported by the National Science Foundation through NSF/DMR-1644779 and 2128556, and the State of Florida. This material is based upon work at the Center for Bioenergy Innovation supported by the U.S. Department of Energy, Office of Science, Biological and Environmental Research under Contract Number ERKP886.

Appendix A. Supplementary data

Supplementary data to this article can be found online at https://doi.org/10.1016/j.ssnmr.2026.102075.

Data availability

Data will be made available on request.

References

[1] S.P. Brown, Applications of high-resolution 1H solid-state NMR, Solid State Nucl. Magn. Reson. 41 (2012) 1–27.
[2] Z. Gan, I. Hung, X. Wang, J. Paulino, G. Wu, I.M. Litvak, P.L. Gor'kov, W.W. Brey, P. Lendi, J.L. Schiano, M.D. Bird, I.R. Dixon, J. Toth, G.S. Boebinger, T.A. Cross, NMR spectroscopy up to 35.2 T using a series-connected hybrid magnet, J. Magn. Reson. 284 (2017) 125–136.
[3] S. Wang, T. Ravula, J.A. Stringer, P.L. Gor'kov, O.A. Warmuth, C.G. Williams, A. F. Thome, L.J. Mueller, C.M. Rienstra, Ultrahigh-resolution solid-state NMR for high–molecular weight proteins on GHz-class spectrometers, Sci. Adv. 11 (2025) eadx6016.
[4] C.M. Quinn, M. Wang, T. Polenova, NMR of macromolecular assemblies and machines at 1 GHz and beyond: new transformative opportunities for molecular structural biology, Methods Mol. Biol. 1688 (2018) 1–35.
[5] V. Martins, J. Xu, I. Hung, Z. Gan, C. Gervais, C. Bonhomme, Y. Huang, 17O solid-state NMR at ultrahigh magnetic field of 35.2 T: resolution of inequivalent oxygen sites in different phases of MOF MIL-53(Al), Magn. Reson. Chem. 59 (2021) 940–950.
[6] S.E. Ashbrook, S. Wimperis, High-resolution NMR of quadrupolar nuclei in solids, Prog. Nucl. Magn. Reson. Spectrosc. 45 (2004) 53–108.
[7] R.W. Dorn, M.C. Cendejas, K. Chen, I. Hung, N.R. Altvater, W.P. McDermott, Z. Gan, I. Hermans, A.J. Rossini, Structure determination of boron-based oxidative dehydrogenation heterogeneous catalysts with ultrahigh field 35.2 T 11B solid-state NMR spectroscopy, ACS Catal. 10 (2020) 13852–13866.
[8] Z. Zhao, D. Xiao, K. Chen, R. Wang, L. Liang, Z. Liu, I. Hung, Z. Gan, G. Hou, Nature of five-coordinated Al in γ-Al2O3 revealed by ultra-high-field solid-state NMR, ACS Cent. Sci. 8 (2022) 795–803.
[9] Q. Wang, W. Li, I. Hung, F. Mentink-Vigier, X. Wang, G. Qi, X. Wang, Z. Gan, J. Xu, F. Deng, Mapping the oxygen structure of γ-Al2O3 by high-field solid-state NMR spectroscopy, Nat. Commun. 11 (2020) 3620.
[10] R.S.K. Madsen, A. Qiao, J. Sen, I. Hung, K. Chen, Z. Gan, S. Sen, Y. Yue, Ultrahigh-field 67Zn NMR reveals short-range disorder in zeolitic imidazolate framework glasses, Science 367 (2020) 1473–1476.
[11] I. Hung, E. Keeler, W. Mao, P.L. Gor'kov, R.G. Griffin, Z. Gan, Residue-specific high-resolution 17O solid-state nuclear magnetic resonance of peptides: multidimensional indirect 1H detection and magic-angle spinning, J. Phys. Chem. Lett. 13 (2022) 6549–6558.
[12] E. Keeler, V.K. Michaelis, M.T. Colvin, I. Hung, P.L. Gor'kov, T.A. Cross, Z. Gan, R. G. Griffin, 17O MAS NMR correlation spectroscopy at high magnetic fields, J. Am. Chem. Soc. 139 (2017) 17953–17963.
[13] J. Paulino, M. Yi, I. Hung, Z. Gan, X. Wang, E.Y. Chekmenev, H. Zhou, T.A. Cross, Functional stability of water wire–carbonyl interactions in an ion channel, Proc. Natl. Acad. Sci. USA 117 (2020) 11908–11915.
[14] E. Nimerovsky, K.T. Movellan, X.C. Zhang, M.C. Forster, E. Najbauer, K. Xue, R. Dervisoglu, K. Giller, C. Griesinger, S. Becker, L.B. Andreas, Proton detected solid-state NMR of membrane proteins at 28 tesla (1.2 GHz) and 100 kHz magic-angle spinning, Biomolecules 11 (2021) 752.
[15] M. Callon, D. Luder, A.A. Malar, T. Wiegand, V. Rimal, L. Lecoq, A. Bockmann, A. Samoson, B.H. Meier, High and fast: NMR protein–proton side-chain assignments at 160 kHz and 1.2 GHz, Chem. Sci. 14 (2023) 10824–10834.
[16] G. Lamon, A. Lends, I. Valsecchi, S.S.W. Wong, V. Duprès, F. Lafont, J. Tolchard, C. Schmitt, A. Mallet, A. Grélard, Solid-state NMR molecular snapshots of Aspergillus fumigatus cell wall architecture during a conidial morphotype transition, Proc. Natl. Acad. Sci. USA 120 (6) (2023) e2212003120.
[17] A.K. Bishoyi, J. van Neer, S. Bahri, S. Lorenz, H. de Cock, M. Baldus, Solid-state NMR reveals reorganization of the Aspergillus fumigatus cell wall due to a host-defence peptide, Angew. Chem. Int. Ed. 64 (2025) e202509012.
[18] M.M. Maricq, J.S. Waugh, NMR in rotating solids, J. Chem. Phys. 70 (1979) 3300–3316.
[19] R.R. Ernst, G. Bodenhausen, A. Wokaun, Principles of Nuclear Magnetic Resonance in One and Two Dimensions, Clarendon Press (Oxford University Press), Oxford, UK, 1990.
[20] M.H. Levitt, Spin Dynamics: Basics of Nuclear Magnetic Resonance, Wiley, Chichester, UK, 2008.
[21] A. Abragam, The Principles of Nuclear Magnetism, Oxford University Press, Oxford, UK, 1961.
[22] F.A. Perras, S. Wang, J. Mayer, M. Halder, A.L. Paterson, D.B. Culver, C. M. Rienstra, Removal of homogeneous broadening from ^{1}H-Detected multidimensional solid-state NMR spectra, Anal. Chem. 97 (2025) 4653–4660.
[23] M. Chavez, T. Wiegand, A.A. Malar, B.H. Meier, M. Ernst, Residual dipolar line width in magic-angle spinning proton solid-state NMR, Magnes. Res. 2 (2021) 499–509.
[24] S. Cadars, A. Lesage, L. Emsley, Chemical shift correlations in disordered solids, J. Am. Chem. Soc. 127 (2005) 4466–4476.
[25] G. Hou, S. Yan, J. Trébosc, J.P. Amoureux, T. Polenova, Broadband homonuclear correlation spectroscopy driven by combined R2(n)(v) sequences under fast magic angle spinning for NMR structural analysis of organic and biological solids, J. Magn. Reson. 232 (2013) 18–30.
[26] G. De Paepe, J.R. Lewandowski, A. Loquet, A. Bockmann, R.G. Griffin, Proton assisted recoupling and protein structure determination, J. Chem. Phys. 129 (2008) 245101.
[27] K.J. Donovan, S.K. Jain, R. Silvers, S. Linse, R.G. Griffin, Proton-assisted recoupling (PAR) in peptides and proteins, J. Phys. Chem. B 121 (2017) 10804–10817.
[28] L.D. Fernando, M.C. Dickwella Widanage, J. Penfield, A.S. Lipton, N. Washton, J. P. Latgé, P. Wang, L. Zhang, T. Wang, Structural polymorphism of chitin and chitosan in fungal cell walls from solid-state NMR and principal component analysis, Front. Mol. Biosci. (8) (2021) 727053.
[29] X. Kang, A. Kirui, A. Muszynski, M.C. Dickwella Widanage, A. Chen, P. Azadi, P. Wang, F. Mentink-Vigier, T. Wang, Molecular architecture of fungal cell walls revealed by solid-state NMR, Nat. Commun. 9 (2018) 2747.
[30] J.R. Yarava, I. Gautam, A. Jacob, R. Fu, T. Wang, Proton-detected solid-state NMR for deciphering structural polymorphism and dynamic heterogeneity of cellular carbohydrates in pathogenic fungi, J. Am. Chem. Soc. 147 (20) (2025) 17416–17432.
[31] A. Safeer, F. Kleijburg, S. Bahri, D. Beriashvili, E.J.A. Veldhuizen, J. van Neer, M. Tegelaar, H. de Cock, H.A.B. Wosten, M. Baldus, Probing cell-surface interactions in fungal cell walls by high-resolution 1H-Detected solid-state NMR spectroscopy, Chem. Eur J. 29 (2022) e202202616.
[32] A. Ankur, J.R. Yarava, I. Gautam, F.J. Scott, F. Mentink-Vigier, C. Chrissian, L. Xie, D. Roy, R.E. Stark, T.L. Doering, Polymorphic α-Glucans as structural scaffolds in cryptococcus cell walls for chitin, capsule, and melanin: insights from ^{13}C and ^{1}H solid-state NMR, Angew. Chem. Int. Ed. 64 (36) (2025) e202510409.
[33] A. Chakraborty, L.D. Fernando, W. Fang, M.C. Dickwella Widanage, P. Wei, C. Jin, T. Fontaine, J.-P. Latgé, T. Wang, A molecular vision of fungal cell wall organization by functional genomics and solid-state NMR, Nat. Commun. 12 (2021) 6346.
[34] P. Rampratap, A. Lasorsa, A. Arunachalam, M. Kamperman, M.T. Walvoort, P. van der Wel, Resolving atomic-level dynamics and interactions of high-molecular-weight hyaluronic acid by multidimensional solid-state NMR, ACS Appl. Mater. Interfaces 16 (2024) 43317–43328.
[35] K. Duong, E. Moss, C. Reichhardt, Solid-state NMR compositional analysis of sputum from people with cystic fibrosis, Solid State Nucl. Magn. Reson. 134 (2024) 101975.
[36] C.H. Byeon, T. Kinney, H. Saricayir, K.H. Hansen, F.J. Scott, S. Srinivasa, M. K. Wells, F. Mentink-Vigier, W. Kim, U. Akbey, Ultrasensitive characterization of native bacterial biofilms via dynamic nuclear polarization-enhanced solid-state NMR, Angew. Chem. Int. Ed. 64 (2025) e202418146.
[37] P. Duan, S. Kaser, J.J. Lyczakowski, P. Phyo, T. Tryfona, P. Dupree, M. Hong, Xylan structure and dynamics in native brachypodium grass cell walls investigated by solid-state NMR spectroscopy, ACS Omega 6 (2021) 15460–15471.
[38] P. Xiao, S. Pfaff, W. Zhao, D. Debnath, C.S. Vojvodin, C.J. Liu, D. Cosgrove, T. Wang, Emergence of lignin-carbohydrate interactions during plant stem maturation visualized by solid-state NMR, Nat. Commun. 16 (2025) 8010.
[39] X. Kang, W. Zhao, M.C. Dickwella Widanage, A. Kirui, U. Ozdenvar, T. Wang, CCMRD: a solid-state NMR database for complex carbohydrates, J. Biomol. NMR 74 (2020) 239–245.
[40] W. Zhao, D. Debnath, I. Gautam, L.D. Fernando, T. Wang, Charting the solid-state NMR signals of polysaccharides: a database-driven roadmap, Magn. Reson. Chem. 62 (2024) 298–309.

[41] D. Li, A.L. Hansen, C. Yuan, L. Bruschweiler-Li, R. Bruschweiler, DEEP picker is a deep neural network for accurate deconvolution of complex two-dimensional NMR spectra, Nat. Commun. 12 (2021) 5229.
[42] F.M. Paruzzo, A. Hofstetter, F. Musil, S. De, M. Ceriotti, L. Emsley, Chemical shifts in molecular solids by machine learning, Nat. Commun. 9 (2018) 4501.
[43] M.C. Dickwella Widanage, I. Gautam, D. Sarkar, F. Mentink-Vigier, J.V. Vermaas, S.-Y. Ding, A.S. Lipton, T. Fontaine, J.-P. Latgé, P. Wang, Adaptative survival of Aspergillus fumigatus to echinocandins arises from cell wall remodeling beyond β−1, 3-glucan synthesis inhibition, Nat. Commun. 15 (2024) 6382.
[44] M. Ernst, A. Samoson, B.H. Meier, Low-power XiX decoupling in MAS NMR experiments, J. Magn. Reson. 163 (2003) 332–339.
[45] F. Schilling, L.R. Warner, N.I. Gershenzon, T.E. Skinner, M. Sattler, S.J. Glaser, Next-generation heteronuclear decoupling for high-field biomolecular NMR spectroscopy, Angew. Chem. Int. Ed. 53 (2014) 4475–4479.
[46] M. Baldus, A.T. Petkova, J. Herzfeld, R.G. Griffin, Cross polarization in the tilted frame: assignment and spectral simplification in heteronuclear spin systems, Mol. Phys. 95 (1998) 1197–1207.
[47] J. Pauli, M. Baldus, B.-J. van Rossum, H. de Groot, H. Oschkinat, Backbone and side-chain 13C and 15N signal assignments of the α-Spectrin SH3 domain by magic angle spinning solid-state NMR at 17.6 tesla, ChemBioChem 2 (2001) 272–281.